Accepted Manuscript

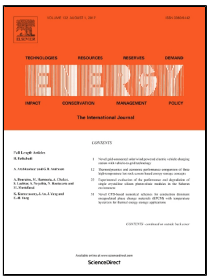

Integrated collector storage solar water heater under partial vacuum

Manolis Souliotis, Spiros Papaefthimiou, Yiannis G. Caouris, Aggelos Zacharopoulos, Patrick Quinlan, Mervyn Smyth

PII:	S0360-5442(17)31450-0
DOI:	10.1016/j.energy.2017.08.074
Reference:	EGY 11443
To appear in:	*Energy*
Received Date:	03 July 2017
Revised Date:	15 August 2017
Accepted Date:	16 August 2017

Please cite this article as: Manolis Souliotis, Spiros Papaefthimiou, Yiannis G. Caouris, Aggelos Zacharopoulos, Patrick Quinlan, Mervyn Smyth, Integrated collector storage solar water heater under partial vacuum, *Energy* (2017), doi: 10.1016/j.energy.2017.08.074

Integrated collector storage solar water heater under partial vacuum

*Manolis Souliotis[1,2,3], Spiros Papaefthimiou[4], Yiannis G. Caouris[5],
Aggelos Zacharopoulos[6], Patrick Quinlan[6], Mervyn Smyth[6]

[1]*Department of Mechanical Engineering, University of Western Macedonia, Greece*
[2]*Department of Environmental Engineering, University of Western Macedonia, Greece*
[3]*Mechanical Engineering Department, Technological Educational Institute of Western Greece,Greece*
[4]*School of Production Engineering and Management, Technical University of Crete, Chania, Greece*
[5]*Department of Mechanical Engineering & Aeronautics, University of Patras, Greece*
[6]*Centre for Sustainable Technologies, Ulster University, Jordanstown, N. Ireland*

Abstract

The work focuses on the experimental study of the heat diode mechanism in an Integrated Collector Storage Solar Water Heater (ICSSWH) for domestic applications. The solar device combines a horizontal cylindrical vessel with an asymmetric reflector trough (Compound Parabolic Concentrator – CPC). The cylindrical storage tank comprises two concentric cylindrical vessels: the outer absorbing vessel and the inner storage vessel. The annulus between the cylindrical vessels is partially depressurized and contains a small amount of water serving as Phase Change Material (PCM), which changes phase (mainly at low temperatures) thus producing vapor and creating a thermal diode transfer mechanism from the outer to the inner surfaces of the vessels. Several experimental results, including uncertainty analysis, are demonstrated through diagrams depicting temperature variations, mean daily efficiency and thermal losses coefficient. Additionally results from the variation of the temperature and the total pressure inside annulus are also presented. The results clearly show that the vapor's pressure plays the most important role regarding the thermal performance of the device.

Keywords: Integrated Collector Storage Solar Water Heaters (ICSSWH); Heat Diode Mechanism; Thermal Behavior; Phase Change Materials (PCM); Compound Parabolic Concentrators (CPC)

*Corresponding author: *Tel/Fax:* +30 24610 56623
E-mail address: msouliotis@uowm.gr (Manolis Souliotis)

1. Introduction

Integrated Collector Storage Solar Water Heaters (ICSSWH) belong to the category of low cost solar devices that mainly cover needs for domestic applications. The development of these systems has been recently discussed in detail in the works of Singh et al [1] and Souliotis et al [2]. However, ICSSWH suffer by ambient heat losses, at nighttime, and extended research activities have been focused on the potential improvement of the thermal behavior in ICS systems by reducing the tank's thermal losses. Smyth et al. [3] studied the thermal properties of different types of integrated collector storage solar water heaters during day and night operation, while Henderson et al. studied the thermal performance of flat plate ICS for various inclinations [4]. The thermal performance of ICS systems can be improved using Compound Parabolic Concentrator (CPC) reflectors. In this category of ICS systems, the solar radiation is reflected and collected on the absorbing surface, while the water tank(s) can be directly connected to the water mains [5-7]. Tripanagnostopoulos et al. [8] and Souliotis et al. [9] studied ICS systems combined with reflectors of symmetrical and asymmetrical CPC geometry while significant articles also include computational and experimental studies [10-15].

Phase Change Materials (PCM) can improve the thermal behavior of solar thermal systems, especially in the case of incorporated storage tanks mainly by reducing thermal losses. Haillot et al. [16] studied a system in which the storage tank was covered with a composite PCM, while Eames and Griffiths [17] presented a numerical study of the thermal behavior of an ICS unit using PCM at 65°C. Griffiths et al. [18] studied experimentally the heat retention of ICS systems using PCM slurries, and similarly, Al-Hinti et al. [19] performed an experimental study of a conventional water heating system using Paraffin wax as PCM. In that work, the system advantage, regarding the hot water availability at higher temperature and over and extended time period, was clearly demonstrated. Recently, Chaabane et al. [20] presented a numerical study of the thermal performance of an ICSSWH with a cylindrical water storage tank (with and without PCM), properly mounted in a CPC reflector. The combination of partial evacuation and PCM in an ICS heater was originally presented in the work of De Beijer [21]. In that work, the evaporator consisted in the collector-absorbing surface and the condenser consisted in

the surface of the inner storage vessel. Pugsley et al. [22] have developed a building integrated hybrid solar ICS water heater working on the same principle achieving instantaneous thermal and electrical efficiencies of 60% and 12%, respectively. Rhee et al. [23] experimentally measured the temperature stratification in a solar hot water storage tank using a double chimney device that acts as a thermal diode. In the work of Souliotis et al. [9] the effective water temperature rise during daily operation and heat retention during nighttime operation, for a device working with respective heat diode mechanisms, was discussed.

In the present work, an ICSSWH comprising two concentric cylindrical vessels (forming an annulus in which water was incorporating as PCM) and an asymmetric CPC reflector, is experimentally studied. The device was designed focusing on the achievement of both highly time response temperature rise of stored water during the day and low nighttime thermal losses. The scope of the work is the investigation of the influence of the vacuum inside the annulus, both in the temperature rise of the stored water during the daily operation and the heat retention during the non-collection period. A detailed experimental study for two consecutive years was accomplished as the next step of previous work published by the authors [9]. Variation diagrams of the stored water temperature and the total pressure within the annulus during 24-hour operation of the device are presented and discussed in detail. Similar diagrams combining the total pressure within the annulus and the vapor temperature, can provide additional information regarding the heat transfer mechanisms. In addition, the variation of both mean daily efficiency and the thermal night losses coefficient for the studied system have been experimentally defined and presented. The paper ends up with comparative experimental results for the ICS device and a commercial Flat Plate Thermosiphonic Unit (FPTU).

2. Description and operation of the ICS experimental model

The experimental unit design was based on an ICS vessel comprising two concentric cylindrical tanks, placed at horizontally orientation inside a truncated CPC reflector trough. The specific reflector scheme was selected in order to maximize the concentration of solar radiation onto the upper surface of the cylindrical tank, and at the same time for the reduction of the heat losses, by convection. The

specified vessel–reflector configuration proposed by Tripanagnostopoulos and Souliotis [8], as illustrated in Fig.1. The tank consists of two concentric cylindrical vessels: the outer absorbing vessel and the inner storage vessel. The annulus between these vessels was partially depressurized and contained a small amount of water (4 kg at 15 °C), acting as PCM which changes phase. The produced vapor creates a thermal diode transfer mechanism, from the outer absorbing surface to the inner storage vessel's surface. Fig. 2 presents the fabricated ICS model at the test field, indicating also some of the used components for the experimental study. The design – construction details and the geometrical analysis for the specific configuration have been presented in a previous work by the authors [9].

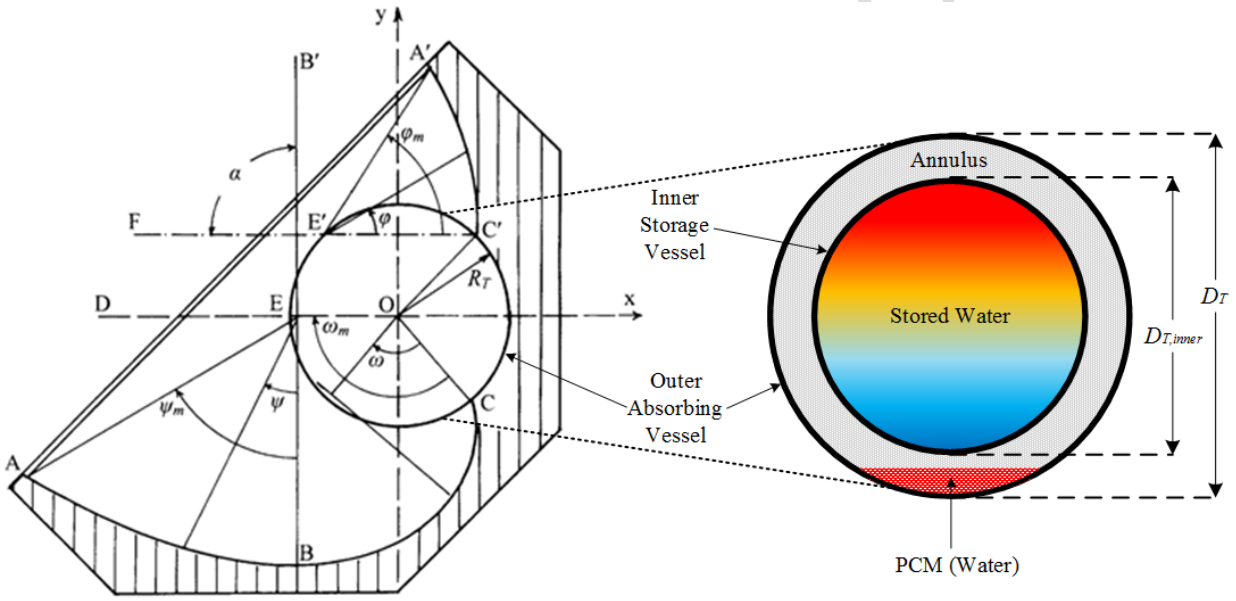

Fig. 1. Cross section of the model and the concentric cylindrical vessels.

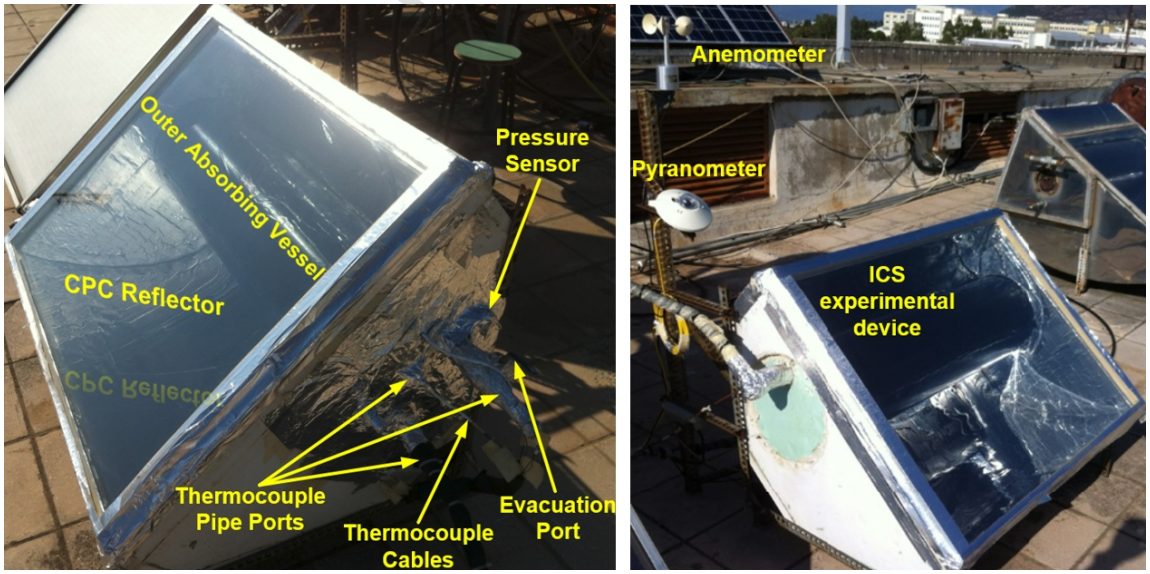

Fig. 2. The ICS experimental device.

3. Experimental set up and method of study

The ICS system was experimentally studied outdoors for the calculation of the mean daily efficiency, η_D) and coefficient of thermal losses, U_S. A CMP6 (Kipp & Zonen) pyranometer, with expected daily uncertainty < 5 % and an A100LK (Windspeed Limited / Vector Instruments) anemometer, with accuracy ± 0.1 m·s^{-1}, were employed to measure the solar radiation G (Wm^{-2}) and the wind speed v_w (ms^{-1}), respectively. For the measurement of the water temperature inside the inner vessel and the vapor temperature in the annulus between the two concentric cylindrical tanks, T type of class 1 copper-constantan (Cu-CuNi) thermocouples, with ± 0.5 °C accuracy, were applied. The total pressure within the annulus was measured by a PMP 4311 (General Electric Measurement & Control) pressure transducer sensor, with ± 2.325 % accuracy (Figs. 2 and 3). The experimental measurements were recorded by using a CR1000 data logger (Campbell Scientific Inc.). In the Appendix a detailed uncertainty analysis is presented, indicating so the accuracies of the involved sensors and logger as the uncertainties of all used magnitudes.

The recording of the stored water temperatures throughout a 24-hour experiment is helpful in order to verify the temperatures stratification day and night. The stratification is important for the estimation of the practical benefits of the whole device. During the day, it is related to the non-uniformity of the absorbed solar radiation [15], as well as the evaporation process of the PCM [9]. The setup that facilitates the effective measuring of relevant water temperatures is achieved by employing a grid of thermocouples suitably positioned inside the inner storage vessel, as indicated in Fig. 3 (positions: plane 1 (1,1), (1,2), (1,3), plane 2: (2,1), (2,2), (2,3) and plane 3: (3,1), (3,2), (3,3), for the measurement of the corresponding temperatures of the stored water: $T_{1,1}$, $T_{1,2}$, $T_{1,3}$, $T_{2,1}$, $T_{2,2}$, $T_{2,3}$, $T_{3,1}$, $T_{3,2}$, and $T_{3,3}$). Within the annulus, three thermocouples were placed in positions (i), (ii) and (iii) (for the measurement of the corresponding vapor temperatures: $T_{v,i}$, $T_{v,ii}$ and $T_{v,iii}$). As indicated in Figs. 2 and 3, the pressure sensor PMP 4311 (pressure's measurement) was installed close to the evacuation port and through the nearest thermocouple pipe port. The recorded parameters: the stored water

temperature: $T_{1,1}$, $T_{2,1}$, $T_{3,1}$ (Bottom), $T_{1,2}$, $T_{2,2}$, $T_{3,2}$ (Middle) and $T_{1,3}$, $T_{2,3}$, $T_{3,3}$ (Up) (all in °C), the temperature of the vapor within the annulus: $T_{v,\mathrm{i}}$, $T_{v,\mathrm{ii}}$, $T_{v,\mathrm{iii}}$, the total pressure within annulus P_{total} (mbar), the ambient temperature T_{α} (°C), the solar irradiance G (Wm^{-2}) and the wind speed v_w (ms^{-1}).

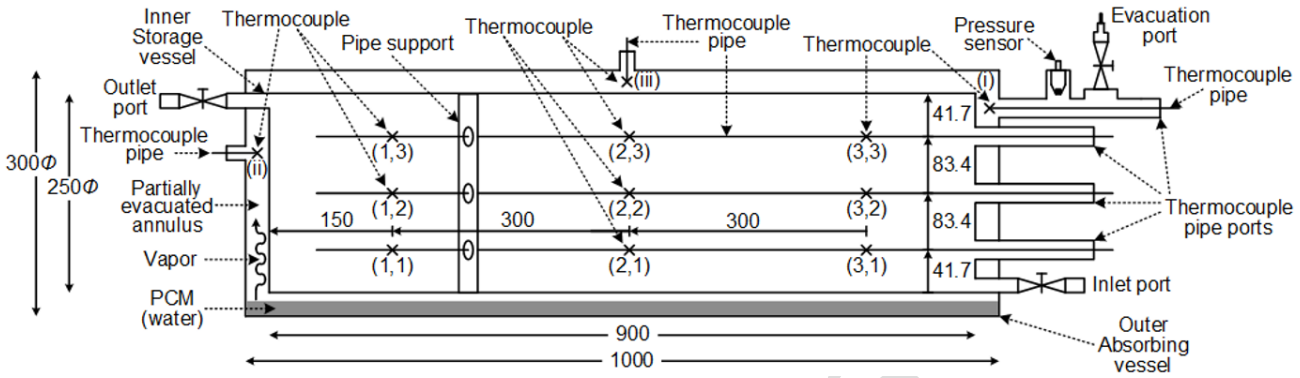

Fig. 3. Cross section of the: inner storage vessel – outer absorbing vessel – numbering / positioning of the thermocouples within the inner storage vessel and the annulus – positioning of the pressure sensor, inlet, outlet, evacuation and thermocouple pipe ports.

The mean temperature of the stored water $T_{w,m}$ (°C) at any time during the operation of the ICS experimental model, was determined using the equation:

$$T_{w,m} = \frac{1}{9} \cdot \left[\sum_{\mathrm{j}=1}^{3} \left(\sum_{\mathrm{i}=1}^{3} T_{\mathrm{i,j}} \right) \right] \tag{1}$$

It varies with seasons and the prevailing weather conditions. The mean water temperatures at the Bottom $T_{1,m}$ (°C), Middle $T_{2,m}$ (°C) and Up $T_{3,m}$ (°C) of the inner vessel were calculated by the equation:

$$T_{\mathrm{j},m} = \frac{1}{3} \cdot \sum_{\mathrm{i}=1}^{3} T_{\mathrm{i,j}} \text{ , for j = 1, 2 and 3} \tag{2}$$

In addition, the mean temperature of the vapor within the annulus $T_{v,m}$ (°C), at any time during the operation of the ICS experimental model, was determined using the equation:

$$T_{v,m} = \frac{1}{3} \cdot \sum_{\mathrm{j}=\mathrm{i}}^{\mathrm{iii}} T_{v,\mathrm{j}} = \frac{1}{3} \cdot \left(T_{v,\mathrm{i}} + T_{v,\mathrm{ii}} + T_{v,\mathrm{iii}} \right) \tag{3}$$

The experimental methodology for the calculation of the mean daily efficiency η_D and thermal losses coefficient during the night-time operation of the system was based on a well-known method [24] which has been extensively implemented in previous published works [5-10], [15], [25], [27, 28].

4. Experimental results and discussion

The experimental study focused on the investigation of the thermal behavior of the device under partial vacuum and at different initial values of the total pressure within the annulus. The main purpose of the experimental procedure was the determination of the time response for the temperature increase of the stored water during the daily operation and the retention of heat during the nighttime operation. The partial vacuum within the annulus affects both the above-mentioned operations [9], [21, 23]. Thus, the experimental results include the 24-hour variation diagrams of all recorded parameters (temperatures, total pressure, solar irradiance, wind speed), in addition to the calculation and the variation diagrams of the mean daily efficiency and the night thermal losses coefficient versus various operational parameters. All the above parameters are measured under partial vacuum for different initial total pressure values in the annulus, while at the same time the corresponding initial temperatures of the water vapor in the annulus and the stored water are recorded as well. For the experimental procedure eight (8) initial values of the total pressure within the annulus (at the lowest temperature possible values of the water-vapor in the annulus) have been chosen: 86 ± 2 mbar (at 19.5 ± 1 °C), 140 ± 3 mbar (at 26.0 ± 1 °C), 245 ± 6 mbar (at 24.0 ± 1 °C), 340 ± 8 mbar (at 25.0 ± 1 °C), 490 ± 11 mbar (at 23.0 ± 1 °C), 670 ± 16 mbar (at 22.0 ± 1 °C), 790 ± 18 mbar (at 20.0 ± 1 °C) and 990 ± 23 mbar (at 24 ± 1 °C). In the above values, the uncertainties for the measurement of the temperature (± 1 °C) and the pressure (± 2.325 %) have been considered according to the uncertainty analysis in the Apendix.

4.1 24-hour operation of the ICS experimental model

The practical benefits from the operation of the tested ICS system are reflected in the temperature variation of the stored water, which is affected by three factors: **i)** the ratio of the total stored water volume per aperture area, **ii)** the distribution of the absorbed solar radiation on the outer vessel [9] and **iii)** the evaporation-condensation process within the annulus between the two concentric cylindrical vessels. The ratio V_T/A_a and the distribution of the absorbed solar radiation on the outer vessel are related to the adopted geometry of the reflectors and it's realization in practice [15]. On the other hand, the total pressure and the temperature of the vapor, dominantly specify the evaporation-condensation process in the annulus, as the pressure and temperature are not independent during phase change processes.

Figures 4A to 8A demonstrate the 24-hour variation profile diagrams of all the involved parameters, i.e. the temperature of the stored water, the temperature of the vapor, the pressure in the annulus, the ambient temperature, the wind speed and the solar radiation intensity. In each figure there is an inset diagram, depicting the time variation of the pressure and the temperature of the vapor, thus providing further necessary information. The initial temperature of the stored water is the lowest possible and hereupon it has been chosen in order to ascertain the maximum stored water temperature rise, during the daily operation. The inset diagrams designate the heat process, indicating the time delay between the maximum values of temperature and pressure of the vapor within the annulus. Figures 4B to 8B depict the variation of the total pressure versus the temperature of the vapor within the annulus. These diagrams present the pressure's time-dependency on temperature (called P-T-t paths) during the dynamically unsteady vaporization-condensation process.

The results show that the observed water temperature stratification is limited. During the day, the non-uniformity of the absorbed solar radiation on the outer vessel seems to have minimal effect on the thermal stratification. During nighttime, the (de)stratification dominantly depends on the thermal convection mechanism within the inner vessel. On the contrary, the temperature rise of the stored water is significant, indicating that the water evaporation in the annulus is crucial. In particular, the lower value of the initial (at 6:30 am) annulus pressure drives to lower temperature difference between the lower (initial at 6:30 am) and maximum temperature of the stored water, during the daily operation of the device (almost at 17:30 pm). For initial pressure of 86 mbar, the temperature difference is near 34 °C while for initial pressure of 990 mbar the corresponding temperature difference is over 42 °C. For intermediate values of the initial pressure, the temperature differences vary almost linearly between the above values. The preservation of the heat during the night, strongly depends on the vapor pressure, as seen by the experimental results. Low pressure leads to low convective heat transfer coefficient in annulus, and subsequently to low temperature differences (17:30 pm until 6:30 am next morning).

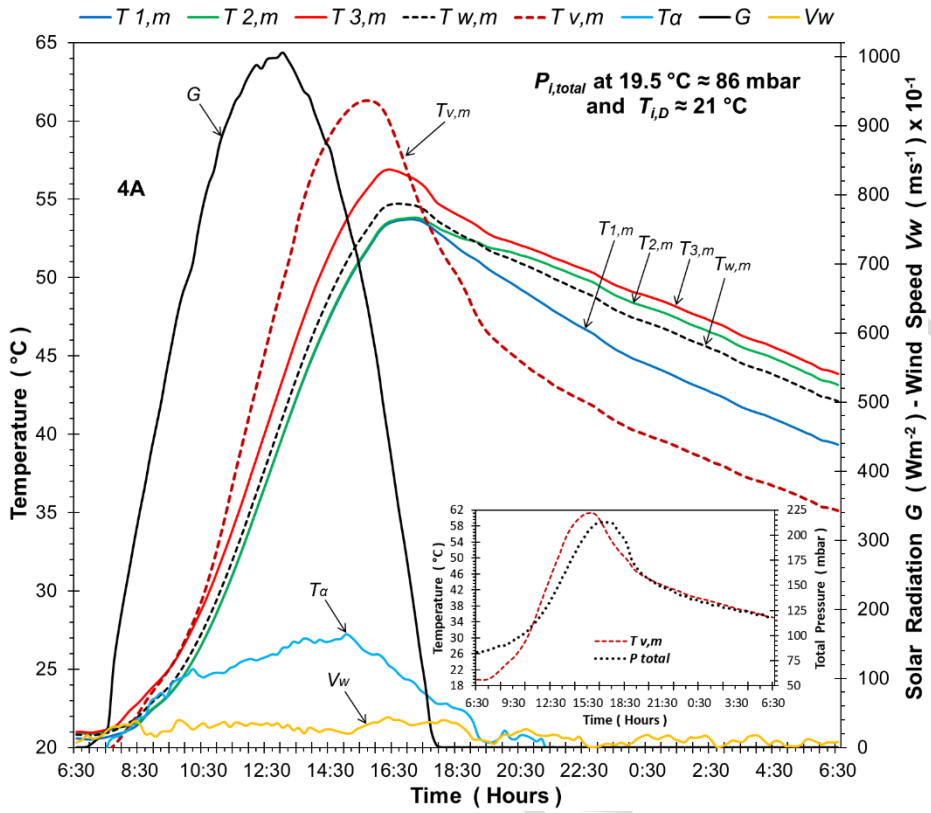

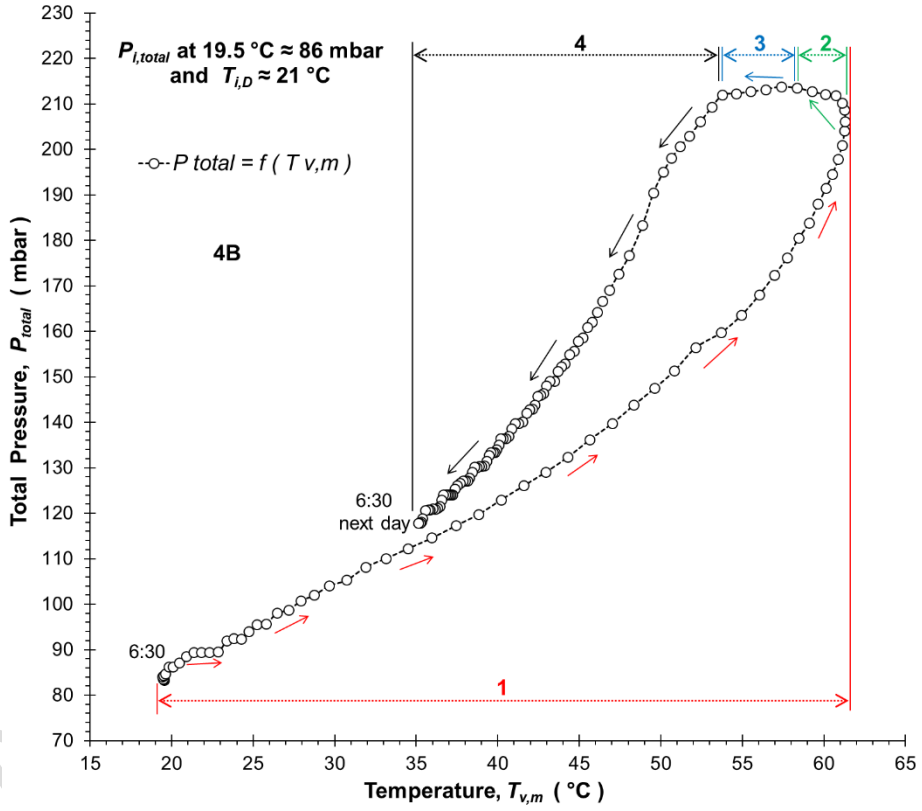

Fig. 4. 4A. Variation in: the mean stored water temperatures within inner storage vessel, the temperature of the vapor and the total pressure within annulus, the ambient temperature, the solar radiation intensity and the wind speed velocity, during the 24-hour test period without draw-off (initial condition, at 06:30: total pressure 86 ± 2 mbar at vapor temperature 19.5 ± 1 °C). 4B. Variation in the total pressure versus the temperature of the vapor within annulus.

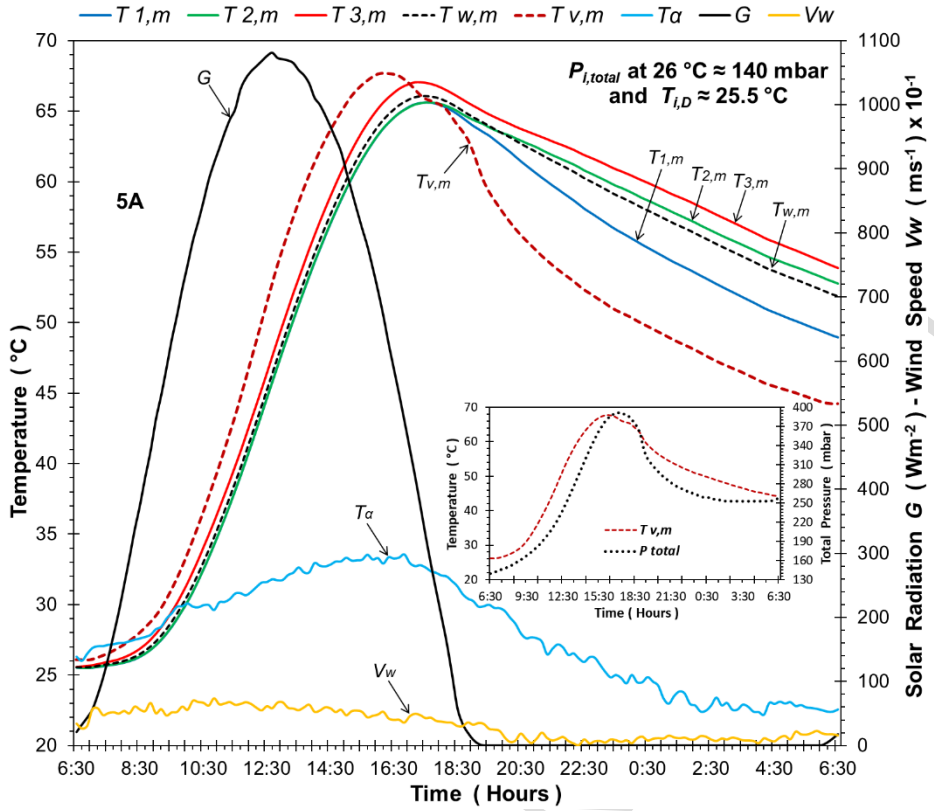

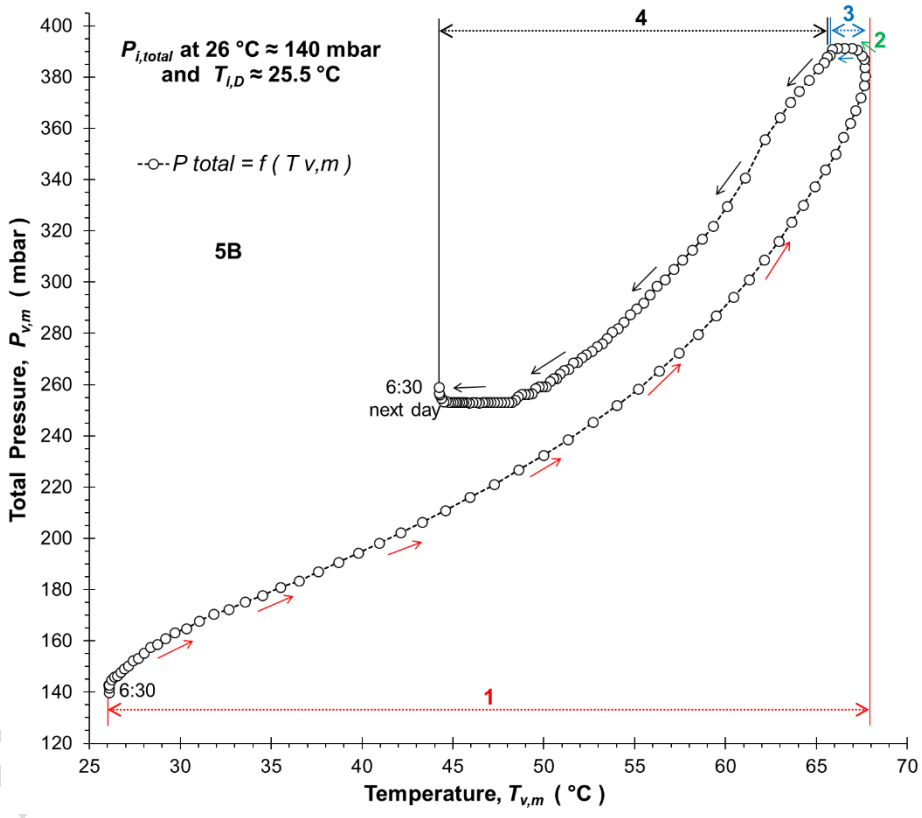

Fig. 5. 5A. Variation in: the mean stored water temperatures within inner storage vessel, the temperature of the vapor and the total pressure within annulus, the ambient temperature, the solar radiation intensity and the wind speed velocity, during the 24-hour test period without draw-off (initial condition, at 06:30: total pressure 140 ± 3 mbar at vapor temperature 26.0 ± 1 °C). 5B. Variation in the total pressure versus the temperature of the vapor within annulus.

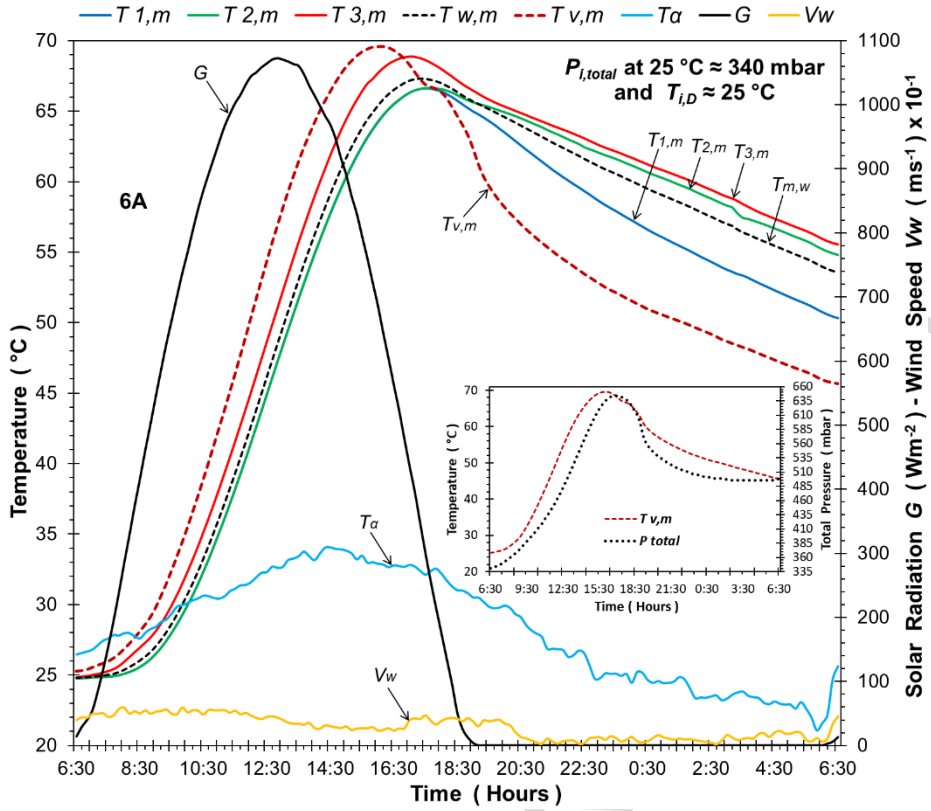

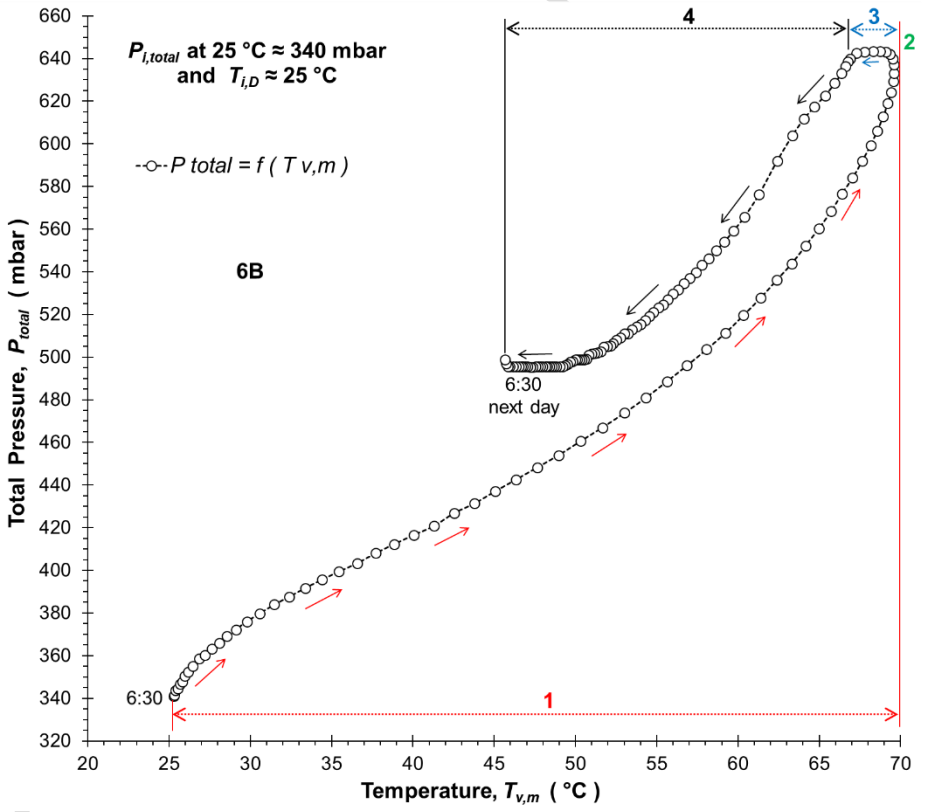

Fig. 6. 6A. Variation in: the mean stored water temperatures within inner storage vessel, the temperature of the vapor and the total pressure within annulus, the ambient temperature, the solar radiation intensity and the wind speed velocity, during the 24-hour test period without draw-off (initial condition, at 06:30: total pressure 340 ± 8 mbar at vapor temperature 25.0 ± 1 °C). 6B. Variation in the total pressure versus the temperature of the vapor within annulus.

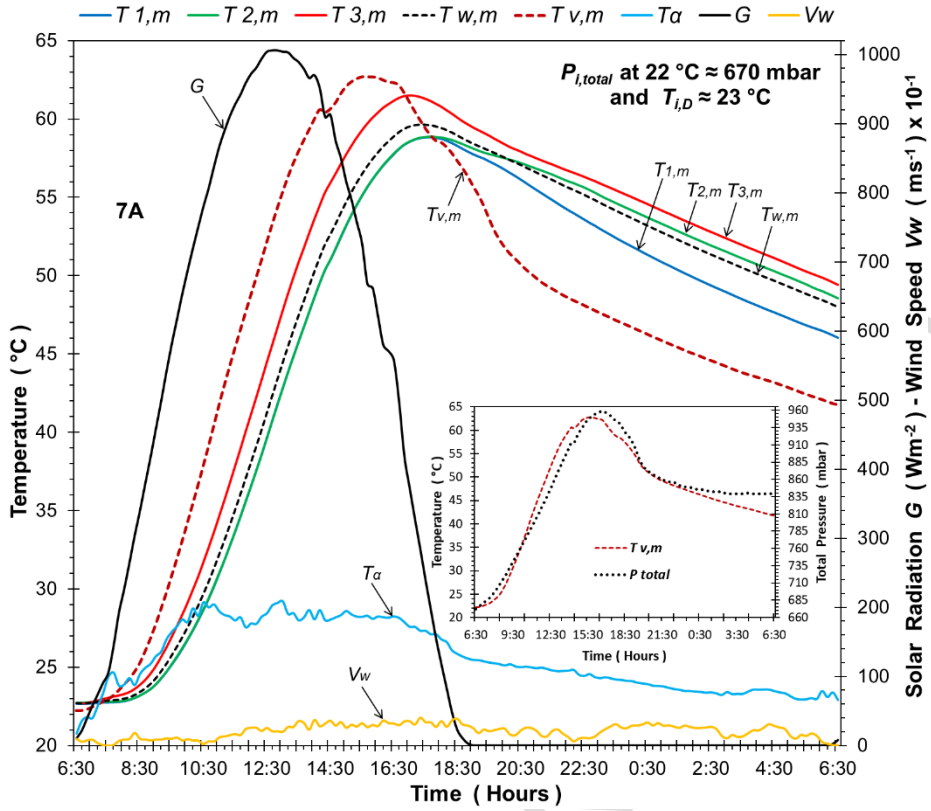

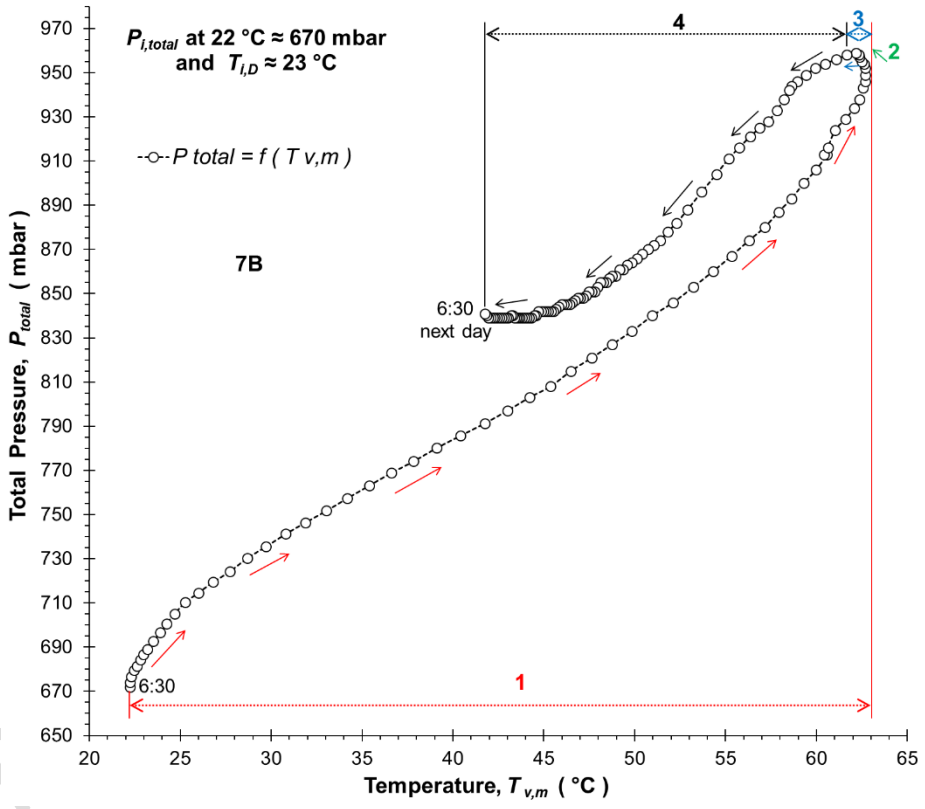

Fig. 7. 7A. Variation in: the mean stored water temperatures within inner storage vessel, the temperature of the vapor and the total pressure within annulus, the ambient temperature, the solar radiation intensity and the wind speed velocity, during the 24-hour test period without draw-off (initial condition, at 06:30: total pressure 670 ± 16 mbar at vapor temperature 22.0 ± 1 °C). 7B. Variation in the total pressure versus the temperature of the vapor within annulus.

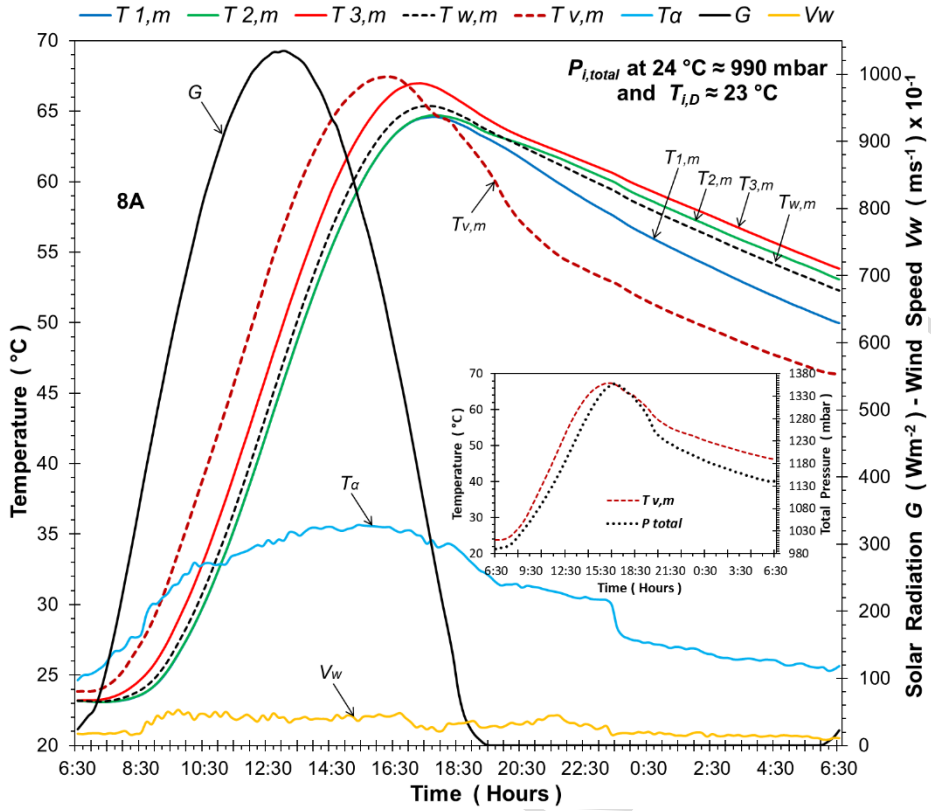

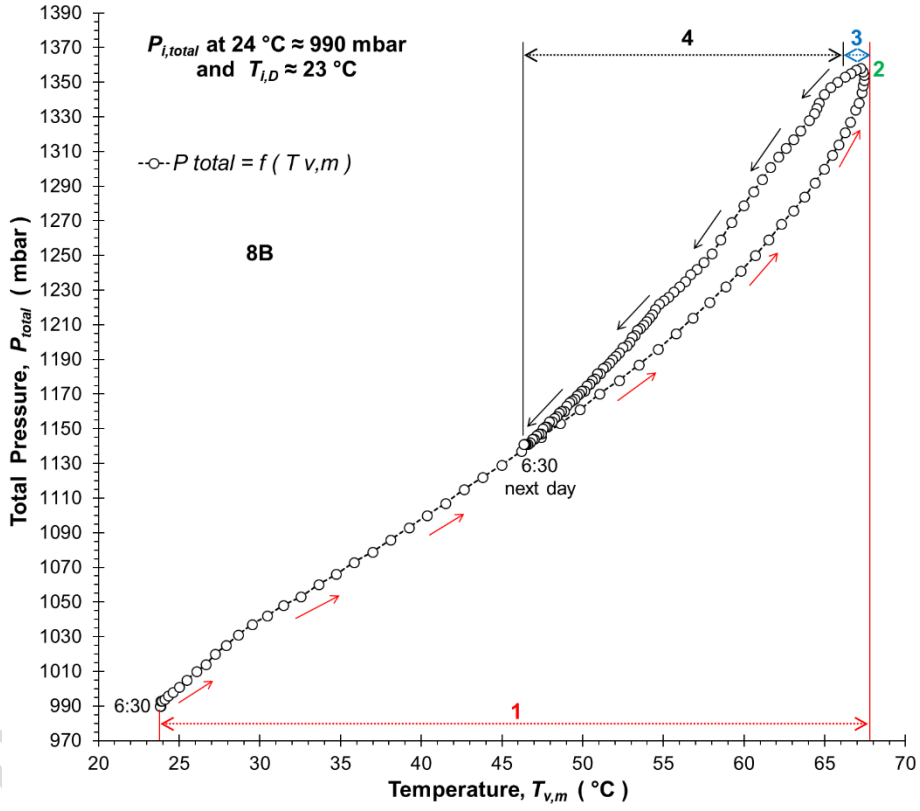

Fig. 8. 8A. Variation in: the mean stored water temperatures within inner storage vessel, the temperature of the vapor and the total pressure within annulus, the ambient temperature, the solar radiation intensity and the wind speed velocity, during the 24-hour test period without draw-off (initial condition, at 06:30: total pressure 990 ± 23 mbar at vapor temperature 24.0 ± 1 °C). 8B. Variation in the total pressure versus the temperature of the vapor within annulus.

Regarding the time response of the temperature rise, the results indicate that the initial pressure within the annulus is not crucial but it depends mainly on the incoming solar radiation. In particular, the time interval between lower and higher values of the stored water temperature, in all initial conditions, is almost the same (~10 hours, at 17:30 pm). There is a constant time delay between the maximum values of the solar radiation intensity and the stored water temperature, almost 5 hours (12:30 pm up to 17:30 pm). Additionally, there is an almost 80 minutes constant time delay between the maximum values of the vapor temperature and the stored water temperature, which depends on the initial pressure.

From the inset diagrams of Figs 4A to 8A, where the time variation of the vapor temperature and pressure are shown, it is evident that there is also a time delay between their maximum values. The results indicate that the time delay decreases as the initial pressure increases (70 minutes in 86 mbar and 20 minutes in 990 mbar). For the initial pressure between the above values, the time delays vary almost linearly between 70 and 20 minutes. There are also differentiations regarding the rise of the total pressure and the temperature of the vapor during the daily operation of the device. As the initial pressure increases, the temperature rises are immediate. This fact determines the actual role of the initial pressure within the annulus during the heating process.

The pressure-temperature variation diagrams of figures 4B to 8B show the time dependency on the heat diode mechanism within the annulus. These diagrams are supplemental to the insets of figures 4A to 8A, and indicate the heating and cooling processes for different initial values of the pressure within the annulus. According to these results, the 24-hour operation of the system is separated into four consecutive processes which are indicated in each of the figures with four numbers: 1, 2, 3 and 4. Process 1 begins at 6:30 in the morning and expires when the temperature of vapor reaches its highest value. During the process 1, both pressure and temperature increase almost linearly up to the time when the solar irradiance is stabilized at its maximum value. Process 2 begins at the end of process 1 and ends when the pressure receives its maximum value, when process 3 begins and ends where the pressure begins to decrease. During this process, the pressure is almost constant and only the temperature of the vapor decreases. Finally, process 4 begins at the end of process 3 and ends at 6:30 in the next morning.

During the last process, both pressure and temperature decrease.

According to the extracted results, processes 2 and 3 almost disappear as the initial pressure within the annulus increases. In particular, process 2 vanishes at initial pressure of 140 mbar, while process 3 almost dies out at initial pressure of 670 mbar. At the pressure of 990 mbar, the whole procedure was practically restricted only to processes 1 and 4. It is worth mentioning the cases when the initial pressure is at 140, 340 and 670 mbar, in which during the process 4 (near 6:30 in the next morning) the pressure is almost constant. At this time range, the results indicate that the system has reached a steady state condition.

The P-T-t paths, for the initial water temperatures above the water mains temperature, seem to be more complicated, as presented in Figure 9, which shows the variation of the pressure versus the vapor temperature for the operation of the device for three continuous days without any storage water temperature reset (draw off). The initial temperature is 40 ± 1 °C and the pressure is almost 870 ± 20 mbar. The figure also includes three inset diagrams where the variation of the parameters for each consequent day of are depicted. The results show that the heating and cooling procedures are practically developed by the processes 1, 2 and 4, as discussed in the previous paragraph. However, there are two additional subjects for discussion. The first refers to the process of heating in which discontinuity regions during process 1 are observed. These discontinuity regions are indicated by black dashed circles in inset diagrams. The discontinuity region is bigger at the third consequent day, compared with the corresponding discontinuities at the first and the second day, when the values of the pressure and the temperature are high. The second subject deals with the intersection points during process 1 and 4 in which they appear for everyone of the 3 days operation of the device and are marked by red solid circles in the inset diagrams. These points are defined by the initial conditions of vapor temperature and pressure and they are located at a constant distance from the maximum temperature during the 24-hour process (almost 16.0 ± 1 °C).

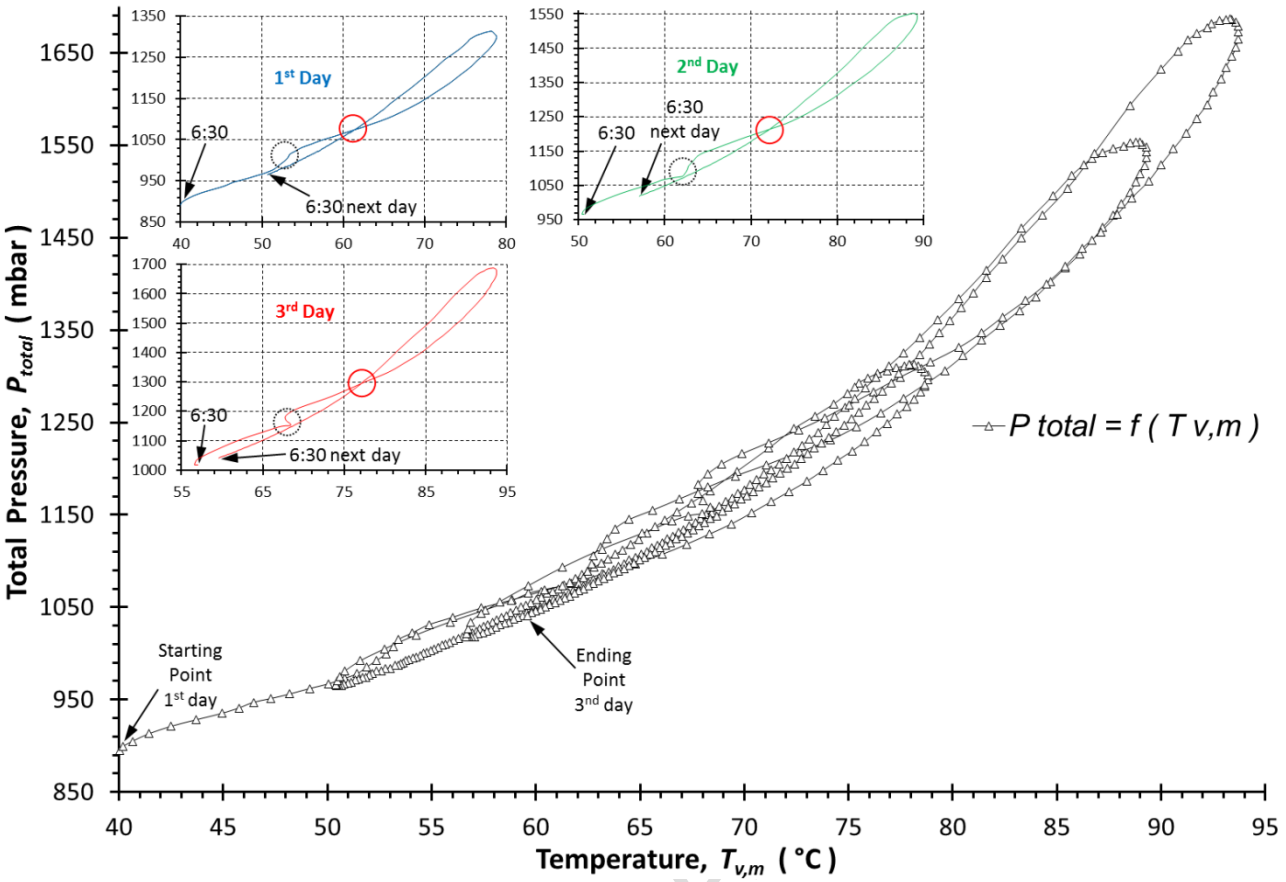

Fig. 9. Variation in the total pressure versus the temperature of the vapor within annulus during 3 continuous days of ICS operation without draw-off (initial conditions at 6:30 in the first day: total pressure 870 ± 20 mbar at vapor temperature 40 ± 1 °C). For the clarification of the thermal performance, inset diagrams depict the variation in the total pressure versus the temperature of the vapor within annulus for each of the three days.

From the above experimental results, it can be deduced that the thermal behavior of the device depends vitally on the initial pressure of the vapor inside the annulus. Concerning the initial conditions at which the device presents the most optimal behavior, it can be concluded that the pressure of the vapor in the range between 670 ± 16 and 790 ± 18 mbar constitutes the more suitable choice. In that range of the initial pressure, the temperature increase, during the daily operation of the device, varies between 37 and 39 °C and at the same time, during nighttime operation, the temperature decrease varies between 11 to 13 °C, which are generally accepted.

4.2 Variation of the mean daily efficiency and thermal loss coefficient

Both the mean daily efficiency and thermal losses coefficient were determined on the basis of consecutive 24-hour operations in which the initial values of the stored water temperatures and partial annulus vacuum were different. Therefore, eight different configurations were studied and thus the total number of the 24-hours experiments arises to almost 100. These experiments were accomplished during the summer period for two consecutive years, and the experimental parameters of the weather conditions (i.e mean solar radiation values, ambient temperature and wind speed) were chosen to be comparable and favorable.

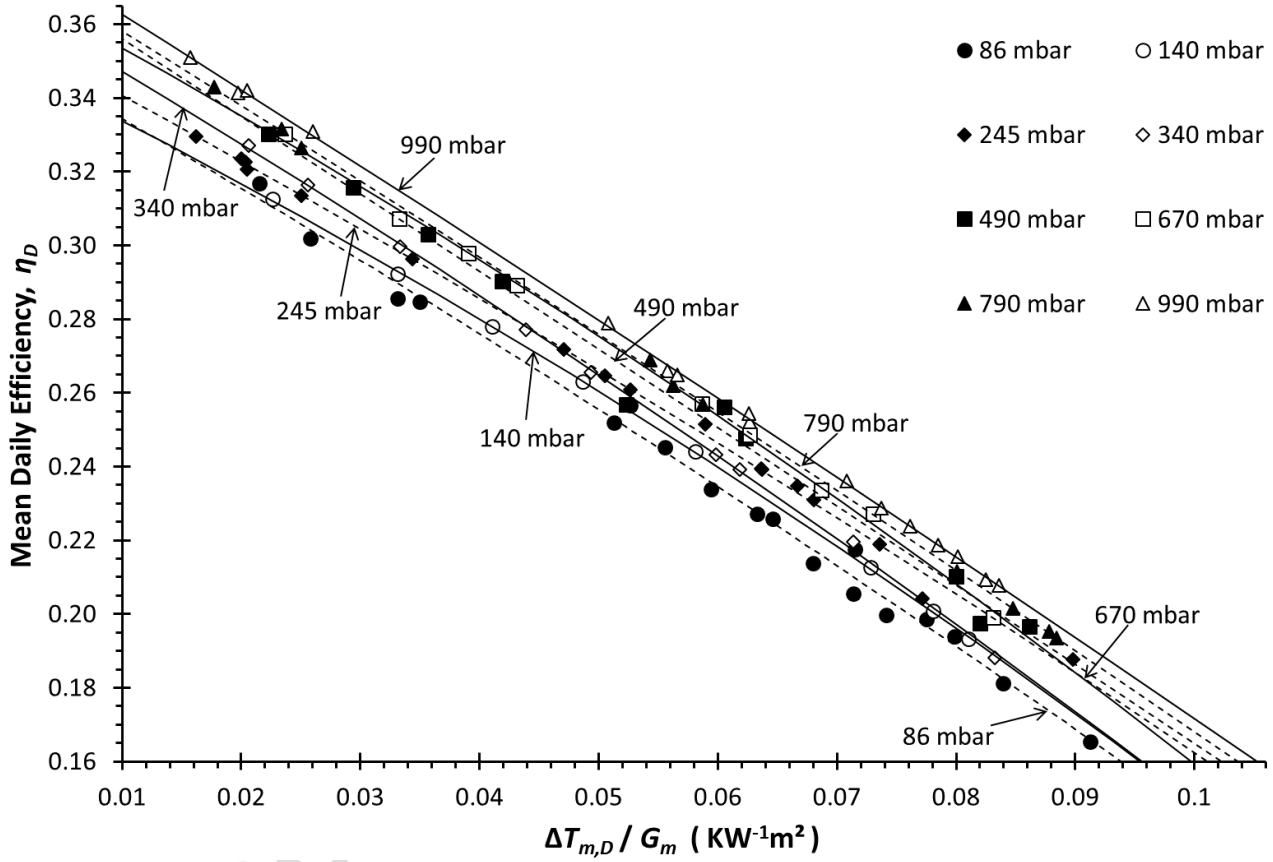

Fig. 10. Variation of the mean daily efficiency η_D of the ICS system, at several initial pressure of partial vacuum, versus $\Delta T_{m,D} / G_m$.

In Fig. 10 the variation in the mean daily efficiency (η_D) for the ICS system versus the parameter $\Delta T_{m,D} / G_m$ ($\Delta T_{m,D} / G_m = \left[\left(T_{i,D} + T_{f,D}\right)/2 - T_{a,D}\right] / G_m$ in K·W^{-1}·m²), are shown for all mentioned cases. The uncertainty for the calculation of the mean daily efficiency η_D has been presented in the Appendix.

For the daily operation of the device, $T_{i,D}$ (°C) is the initial temperature of the stored water 6 hours before solar noon (at ~ 6:30 in the morning), $T_{f,D}$ (°C) is the final temperature of the stored water 6 hours after solar noon (at ~18:30 in the afternoon) and $T_{a,D}$ (°C) is the mean ambient temperature during the daily operation, according ISO 9459-2 [24]. For $\Delta T_{m,D} / G_m$ values ranging between 0.0150 ± 0.0002 and 0.045 ± 0.002 $K \cdot W^{-1} \cdot m^2$, the ICS system behaves better as the initial pressure increases, while the best performance is observed for initial pressure of 990 mbar. This is in agreement with the results presented in the previous section, in which the initial temperature of the stored water varies at low values. In the range between 0.045 ± 0.002 and 0.075 ± 0.004 $K \cdot W^{-1} \cdot m^2$ the thermal performance of the device indicates that for initial pressure of 990 mbar the device still behaves better than the rest configurations, but also for 490, 670 and 790 mbar the mean daily efficiencies of the device are quite similar. It is important to be noticed that this operational range can be considered as typical for the ICS system, as the mean stored water temperature during the daily operation varies between 35 and 60 °C. For the operational range between 0.075 ± 0.004 and 0.090 ± 0.005 $K \cdot W^{-1} \cdot m^2$ the values of the mean daily efficiencies, at the initial pressure of 990 mbar, are higher than the corresponding values in other cases. However, the mean daily efficiencies at the initial pressures of 245, 490, 670 and 790 mbar are almost equal, approaching the corresponding value for the initial pressure of 990 mbar. In Table 1 equations of the mean daily efficiency η_D and their regression coefficient *R*, for all studied cases of the tested device, against $\Delta T_{m,D} / G_m$, are also depicted.

Table 1

Correlations for mean daily efficiency η_D, including the Regression Coefficient *R*, for initial values of total partial vacuum pressure (at specific temperatures), versus $\Delta T_{m,D} / G_m$.

Initial total pressure of partial vacuum (at temperature)	Mean daily efficiency, η_D	Regression Coefficient, R
86 ± 2 mbar (at 19.5 ± 1°C)	$0.353 - 1.823 \cdot \left(\Delta T_{m,D} / G_m\right) - 2.476 \cdot \left(\Delta T_{m,D} / G_m\right)^2$	0.9964
140 ± 3 mbar (at 26.0 °C ± 1°C)	$0.350 - 1.574 \cdot \left(\Delta T_{m,D} / G_m\right) - 4.356 \cdot \left(\Delta T_{m,D} / G_m\right)^2$	0.9999
245 ± 6 mbar (at 24.0 ± 1°C)	$0.358 - 1.716 \cdot \left(\Delta T_{m,D} / G_m\right) - 2.389 \cdot \left(\Delta T_{m,D} / G_m\right)^2$	0.9988
340 ± 8 mbar (at 25.0 ± 1°C)	$0.367 - 1.894 \cdot \left(\Delta T_{m,D} / G_m\right) - 2.780 \cdot \left(\Delta T_{m,D} / G_m\right)^2$	0.9997
490 ± 11 mbar (at 23.0 ± 1°C)	$0.377 - 2.091 \cdot \left(\Delta T_{m,D} / G_m\right) - 0.300 \cdot \left(\Delta T_{m,D} / G_m\right)^2$	0.9954
670 ±16 mbar (at 22.0 ± 1°C)	$0.371 - 1.720 \cdot \left(\Delta T_{m,D} / G_m\right) - 3.981 \cdot \left(\Delta T_{m,D} / G_m\right)^2$	0.9993
790 ±18 mbar (at 20.0 ± 1°C)	$0.378 - 1.986 \cdot \left(\Delta T_{m,D} / G_m\right) - 1.143 \cdot \left(\Delta T_{m,D} / G_m\right)^2$	0.9999
990 ± 23 mbar (at 24.0 ± 1°C)	$0.383 - 2.019 \cdot \left(\Delta T_{m,D} / G_m\right) - 0.939 \cdot \left(\Delta T_{m,D} / G_m\right)^2$	0.9999

Figure 11 presents the variation of the thermal loss coefficient U_S (W·K^{-1}) during nighttime operation of the ICS system, versus the parameter $\Delta T_{m,N}$ ($\Delta T_{m,N} = T_{i,N} - T_{a,N}$) (K). During nighttime operation, $T_{i,N}$ (°C) is the initial temperature of the stored water 6 hours after solar noon (at ~18:30 in the afternoon) and $T_{a,N}$ (°C) is the mean ambient temperature during the nighttime operation. The uncertainty for the calculation of the thermal loss coefficient U_S has been presented in the Appendix.

The thermal loss coefficient ranged from 1.30 ± 0.02 to 1.70 ± 0.02 W·K^{-1} for all configurations. The ICS experimental system at 990 mbar exhibits the highest thermal loss coefficient values (~1.67 ± 0.02 W·K^{-1}), in the total range of $\Delta T_{m,N}$, compared to the corresponding values in all other cases. In the range of $\Delta T_{m,N}$ between 25 and 45 °C for initial pressure of 86 mbar, the device presents the lowest thermal loss coefficient values (1.30 ± 0.02 to 1.54 ± 0.02 W·K^{-1}). For intermediate values of the initial pressure and for the same operational range, the corresponding thermal losses vary between a minimum (at 86 mbar) and a maximum (at 990 mbar). In the range between 45 and 70 °C, the difference in the

variation of the thermal losses coefficient for all cases are almost the same as in the range between 25 and 45 °C, except for the case at the initial pressure of 670 mbar, at which the thermal losses coefficient is almost constant (varies between 1.60 ± 0.02 to 1.62 ± 0.02 W·K^{-1}). It is worth mentioning the variation of the thermal losses coefficient for the cases 86 and 140 mbar at which the increase rate of the thermal losses is significantly higher than the corresponding rate for the other configurations. According to the above results, the selection of initial pressure of 670 mbar seems to be the most suitable choice.

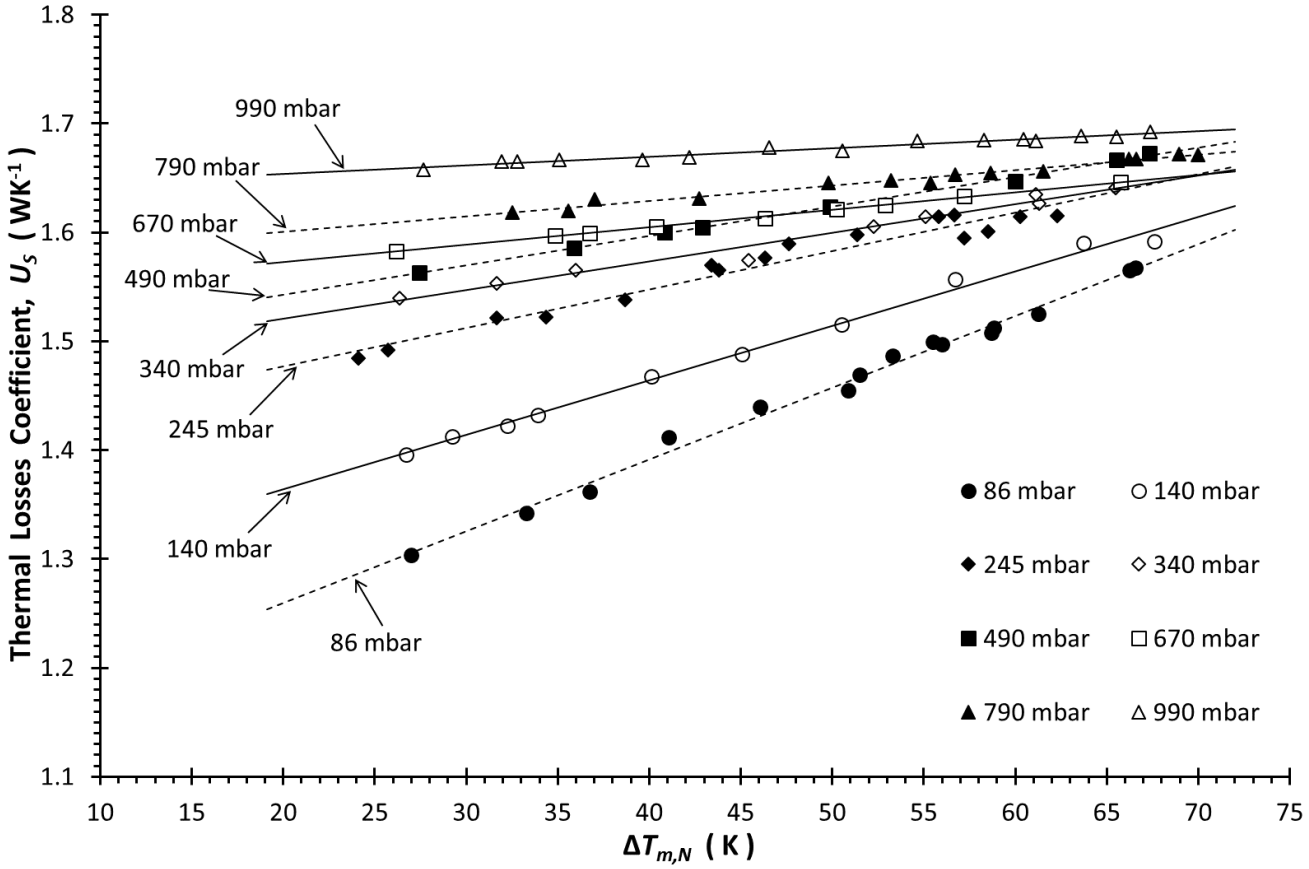

Fig. 11. Variation of the thermal loss coefficient U_S for the ICS system, at several initial pressure of partial vacuum, versus $\Delta T_{m,N}$.

It is noteworthy that the present results give strong evidence that the thermal loss coefficients for the ICS model under consideration, for all cases, exhibit lower values as compared to existing literature [1, 2]. This can be considered as a very significant improvement for this type of solar devices. Table 2 contains the fitting equations of U_S for all studied cases, including their regression coefficient *R*, against $\Delta T_{m,N}$.

Table 2

Correlations for thermal loss coefficient U_S, including the Regression Coefficient *R*, for initial values of total partial vacuum pressure (at specific temperatures), versus $\Delta T_{m,N}$.

Initial total pressure of partial vacuum (at temperature)	Thermal loss coefficient, U_S (WK^{-1})	Regression Coefficient, R
86 ± 2 mbar (at 19.5 ± 1°C)	$1.128 + 0.0066 \cdot \Delta T_{m,N}$	0.9966
140 ± 3 mbar (at 26.0 °C ± 1°C)	$1.264 + 0.0050 \cdot \Delta T_{m,N}$	0.9971
245 ± 6 mbar (at 24.0 ± 1°C)	$1.407 + 0.0035 \cdot \Delta T_{m,N}$	0.9775
340 ± 8 mbar (at 25.0 ± 1°C)	$1.468 + 0.0026 \cdot \Delta T_{m,N}$	0.9897
490 ± 11 mbar (at 23.0 ± 1°C)	$1.489 + 0.0027 \cdot \Delta T_{m,N}$	0.9990
670 ±16 mbar (at 22.0 ± 1°C)	$1.541 + 0.0016 \cdot \Delta T_{m,N}$	0.9994
790 ±18 mbar (at 20.0 ± 1°C)	$1.573 + 0.0014 \cdot \Delta T_{m,N}$	0.9879
990 ± 23 mbar (at 24.0 ± 1°C)	$1.638 + 0.0008 \cdot \Delta T_{m,N}$	0.9805

As mentioned above, the thermal behavior of the system defined substantially by the values of mean daily efficiency, in the typical operational range between 0.075 ± 0.004 and 0.090 ± 0.005 $K \cdot W^{-1} \cdot m^2$ and the values of thermal loss coefficient in the typical operational range between 45 and 70 °C. Conclusively, taking into account the overall performance, according to the 24-hour operation and the variations of the mean daily efficiency and the night thermal losses coefficient, the ICS model with initial pressure of 670 ± 16 mbar behaves at an optimal level. However, further improvement with regard to thermal performance could be achieved by optimizing or accelerating the thermal diode transfer mechanism.

4.3 Comparative experimental results between the ICS model and FPTU system

Since FPTU and ICS solar water heaters belong to the category of solar devices that cover needs of domestic applications, a recent comparative study has been accomplished [29]. In the present work, for the determination of the practical benefits of the studied ICS model, an additional experimental procedure has been realized. In particular, its thermal behavior of was compared to that of a commercial FPTU. The flat heat receiver was covered with a selective coating (with $\alpha_r = 0.92$ and $\varepsilon_r = 0.15$), whilst the stored water volume and the aperture area were $V_T = 96.00 \pm 0.01$ l and $A_\alpha = 1.77 \pm 0.01$ m², respectively. Thus the ratio of stored water volume to the aperture area is $V_T / A_\alpha = 54.360 \pm 0.014$ lm^{-2}. It should be noted that that this ratio is almost the same as in the ICS experimental model (53.420 ± 0.014 lm^{-2}) [9], thus validating the comparison of the temperature/time behavior amongst the two systems. The uncertainty for the measurement of the ratio V_T / A_α has been calculated in the Appendix. The temperature stratification was measured by three (3) thermocouples ($T_{1\ \mathrm{FPTU}}$, $T_{2\ \mathrm{FPTU}}$ and $T_{3\ \mathrm{FPTU}}$) which were suitably placed in lower, middle and upper part of the tank.

In Figure 12 four comparative 24-hour variation diagrams in the stored water temperatures for the ICS and the FPTU systems without draw-off are presented. The experimental process started for both systems with initial mean water temperatures around 23 °C while the ICS was set up at different initial pressure inside the annulus each time. For each diagram there is an inset indicating the variation of the mean temperature of the stored water for both systems. In Fig. 12A the initial pressure inside the annulus was 86 mbar, while in Figs 12B, 12C and 12D the corresponding initial pressures were 340, 670 and 990 mbar. As indicated in all figures, the water temperature of the FPTU system varies in the same range (between 23 and almost 70 °C). On the contrary, the corresponding temperature variation of the ICS system depends on the initial pressure inside the annulus. In addition, the preservation of heat for the FPTU system is almost constant, but for the ICS system this depends also on the initial pressure inside the annulus. From the experimental results, it is obvious that during the daily operation, the ICS system with initial pressure of 990 mbar has a better performance compared to the remaining cases and it approaches the performance of the FPTU system. Conversely, as the initial pressure drops down, the

preservation of the heat increases. Inset diagrams in all cases show the same results. The ICS device (at initial pressures 670 and 990 mbar) operates slightly better than the FPTU in the early morning when the initial water temperature of both systems is around 23 °C. A direct comparison of the two systems indicates that the temperature stratification of ICS system, in all cases, is enhanced compared to the FPTU one. Taking into consideration so the temperature increase, during the daily operation of the ICS system, as the heat preservation, during the nighttime operation of it, the initial pressure around 670 mbar represents the best choice among the rest cases.

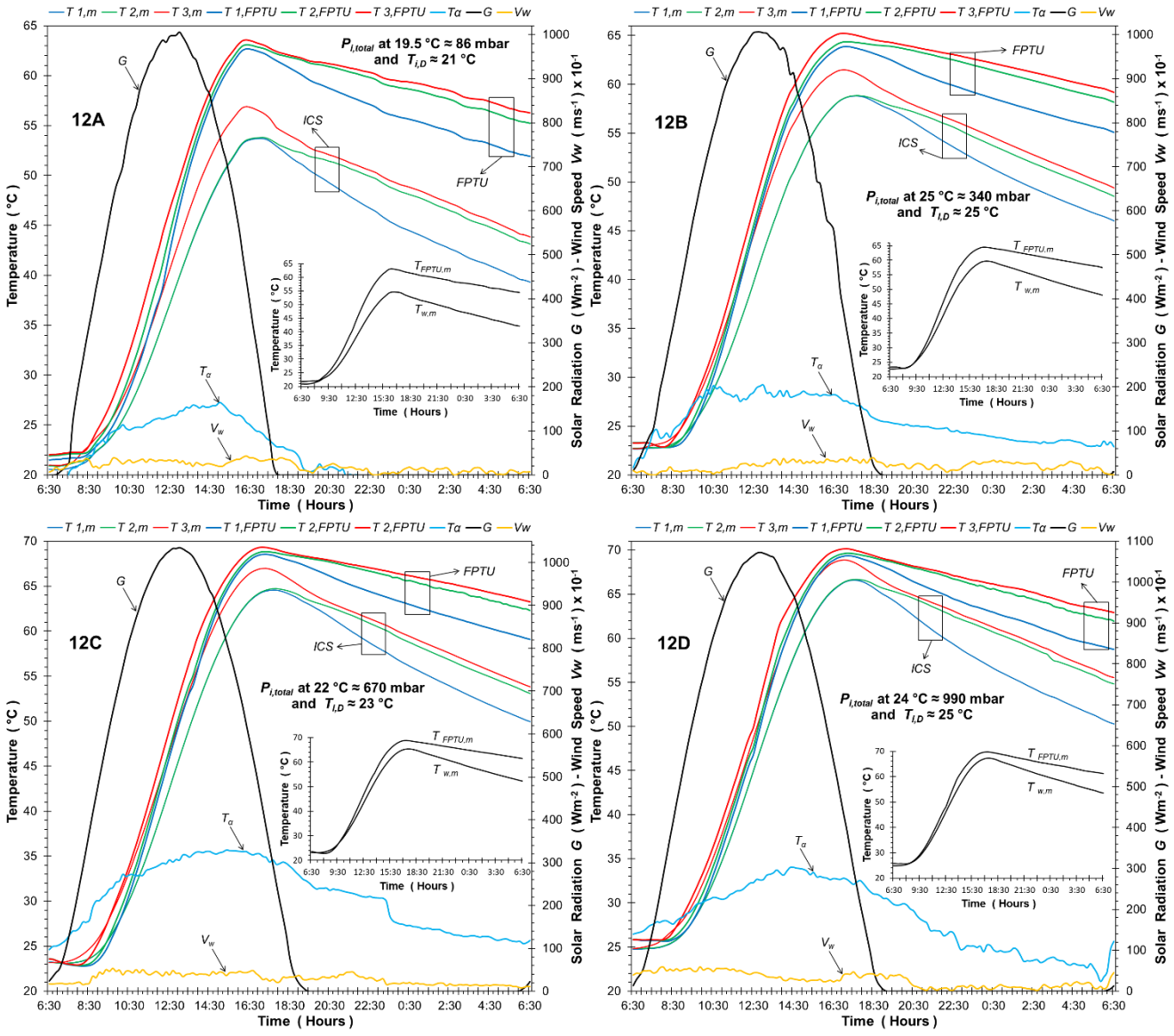

Fig. 12. Comparative 24 hour variation diagrams in the stored water temperatures of ICS and FPTU systems without draw-off at initial (06:30) mean water stored temperature, for both devices, in the range between 21 – 25 ± 1 °C. Variation diagrams in ambient temperature, solar radiation intensity and wind speed velocity. Inner diagrams show the 24-hour variation diagrams in the mean stored water temperatures of ICS and FPTU.

5. Conclusions

A systematic and extensive experimental study of an ICS system, which comprises of two horizontal concentric cylinders combined with a stationary truncated asymmetric CPC reflector trough, has been performed in a time frame spanning more than two years. The novelty of the suggested working principle is that, inside the annulus, a thermal diode mechanism was introduced with the aid of a PCM material, while the area was partially depressurized. Our results indicate that despite of the non-uniformity of the absorbed radiation, the temperature stratification of stored water is marginal. The operation of the solar device is determined by the effectiveness of the thermal diode mechanism, with the PCM vapor pressure being the crucial parameter. The results showed that the ICS system operates at an optimal level when the initial pressure within annulus in the pressure located closed to 670 mbar. The optimal thermal behavior of the device has to do mainly with the significant temperature increase (around 37 °C) during its daily operation in combination with the low values of night thermal loss coefficient, in which is varied in the range between 1.60 to 1.62 $W \cdot K^{-1}$. These two findings can be considered significant improvements for the ICS systems. Additionally, the comparison of the thermal behavior between the ICS device and a commercial FPTU reveals an improved thermal performance of the ICS system, offering an alternative solution for water heating. The present study might serve as a model for future experiments with different PCM materials and variable design/geometry parameters.

Acknowledgments

The authors gratefully acknowledge COST Action TU1205 “Building Integrated Solar Thermal Systems” for providing excellent research networking. Dr. Souliotis also would like to acknowledge the Greek PPC (Public Power Corporation S.A. - Hellas) for the financial support.

References

[1] Singh R, Lazarus IJ, Souliotis M. Recent developments in integrated collector storage (ICS) solar water heaters: A review. Renewable & Sustainable Energy Reviews 2016; 54: 270–298.

[2] Souliotis M, Singh R, Papaefthimiou S, Lazarus IJ, Andriosopoulos K.. Integrated Collector Storage Solar Water Heaters: Survey and Recent developments. Energy Systems 2016; 7: 49–72.

[3] Smyth M, McGarrigle P, Eames PC, Norton B. Experimental Comparison of Alternative Convection Suppression Arrangements for Concentrating Integral Collector Storage Solar Water Heaters. Solar Energy 2005; 78: 223-233.

[4] Henderson D, Junaidi H, Muneer T, Grassie T, Currie J. Experimental and CFD investigation of an ICSSWH at various inclinations. Renewable and Sustainable Energy Reviews 2007; 11: 1087-1116.

[5] Tripanagnostopoulos Y, Souliotis M. ICS solar systems with two water tanks. Renewable Energy 2006; 31: 1698-1717.

[6] Tripanagnostopoulos Y, Souliotis M, Nousia Th. CPC Type Integrated Collector Storage Systems. Solar Energy 2002; 72: 327-350.

[7] Souliotis M, Tripanagnostopoulos Y. Experimental Study of CPC type ICS solar systems. Solar Energy 2004; 76: 389-408.

[8] Tripanagnostopoulos Y, Souliotis M. Integrated Collector Storage Solar Systems with Asymmetric CPC Reflectors. Renewable Energy 2004; 29: 223-248.

[9] Souliotis M, Quinlan P, Tripanagnostopoulos Y, Smyth M, Zacharopoulos A, Ramirez M, Yianoulis P. Heat retaining integrated collector storage system with asymmetric CPC reflector. Solar Energy 2011; 85: 2474-2487.

[10] Souliotis M, Kalogirou S, Tripanagnostopoulos Y. Modelling of an ICS solar water heater using Artificial Neural Networks and TRNSYS. Renewable Energy 2009; 34: 1333-1339.

[11] Helal O, Chaouachi S, Gabsi S. Design and thermal performance of an ICS solar water heater based on three parabolic sections. Renewable Energy 2011; 85: 2421-2432.

[12] Gertzos K, Caouris Y. Experimental and computational study of the developed flow field in a flat plate integrated collector storage (ICS) solar device with recirculation. Experimental Thermal and Fluid Science 2007; 31: 1133-1145.

[13] Garnier C, Currie J, Muneer T. Integrated collector storage solar water heater: Temperature stratification. Applied Energy 2009; 86: 1465-1469.

[14] Kumar R, Rosen M. Integrated collector - storage solar water heater with extended storage unit. Applied Thermal Engineering 2011; 31: 348-354.

[15] Souliotis M, Tripanagnostopoulos Y. Study of the distribution of the absorbed solar radiation on the performance of a CPC type ICS water heater. Renewable Energy 2008; 33: 846-858.

[16] Haillot D, Py X, Goetz V, Benabdelkarim M. Storage composites for the optimisation of solar water heating systems. Chemical Engineering Research and Design 2008; 86: 612-617.

[17] Eams PC, Griffiths PW. Thermal behaviour of integrated solar collector/storage unit with 65°C phase change material. Energy Conversion and Management 2006; 47: 3611-3618.

[18] Griffiths PW, Huang MJ, Smyth M. Improving the heat retention of integrated collector/storage solar water heaters using Phase Change Materials Slurries. International Journal of Ambient Energy 2007; 28: 89-98.

[19] Al-Hinti I, Al-Ghandoor A, Maaly A, Abu Naqeera I, Al-Khateeb Z, Al-Sheikh O. Experimental investigation on the use of water-phase change material storage in conventional solar water heating systems. Energy Conversion and Management 2010; 51: 1735-1740.

[20] Chaabane M, Mhiri H, Bournot P. Thermal performance of an integrated collector storage solar water heater (ICSSWH) with phase change materials (PCM). Energy Conversion and Management 2014; 78: 897–903.

[21] De Beijer HA. Product development in solar water heating. Proceedings of the 5th World Renewable Energy Congress 1998; Florence, Italy: 201-204.

[22] Pugsley A, Smyth M, Mondol J, Zacharopoulos A, Mattia L. Experimental characterisation of a flat panel integrated collector-storage solar water heater featuring a photovoltaic absorber and a planar liquid-vapour thermal diode. EuroSun 2016; Spain, 11–14 October 2016.

[23] Rhee J, Campbell A, Mariadass A, Morhous B. Temperature stratification from thermal diodes in solar hot water storage tank. Solar Energy 2010; 84: 507–511.

[24] Solar heating — Domestic water heating systems — Part 2: Outdoor test methods for system performance characterization and yearly performance prediction of solar-only systems. ISO 9459-2:1995. www.iso.org.

[25] Caouris YG, Souliotis M. Examination of top and bottom inlet position in horizontal mantle heat exchanger solar thermosiphonic circuits. International Journal of Sustainable Energy 2013; 32: 421-433.

[26] Aranovitch E, Gilliaert D, Gillett WB, Bates JE. Test methods for solar water heating systems. In Proceedings of 5th meeting of European Solar Collector and Systems Group, Seville, Spain, (1986); 149-194.

[27] Tripanagnostopoulos Y, Souliotis M. ICS solar systems with horizontal cylindrical storage tank and reflector of CPC or involute geometry. Renewable Energy 2004; 29: 13–38.

[28] Tripanagnostopoulos Y, Souliotis M. ICS solar systems with horizontal (E–W) and vertical (N–S) cylindrical water storage tank. Renewable Energy 2004; 29: 73–96.

[29] Arnaoutakis N., Souliotis M., Papaefthimiou S. Comparative experimental life cycle assessment of two commercial solar thermal devices for domestic applications. Renewable Energy 2017; 111: 187-200.

APPENDIX: Uncertainty analysis

The characteristics of the instrumentation used, for the measurement of various magnitudes, are:

- *Temperature:* by T type class 1 thermocouples, with ± 0.5°C accuracy.
- *Irradiation:* by a CMP6 (Kipp & Zonen) pyranometer, with expected daily uncertainty < 5%
- *Wind speed:* by an A100LK (Windspeed Limited / Vector Instruments) anemometer, with accuracy ± 0.1 $m \cdot s^{-1}$ (in the range between 1 and 10 $m \cdot s^{-1}$). The wind speed is not involved in the uncertainty calculations, as it consists an indicative measure, for the comparativeness of results.
- *Total pressure within the annulus:* by a PMP 4311 (General Electric Measurement & Control) pressure transducer sensor, with ± 2.325% accuracy (see below).
- *Aperture area:* It is assumed an accuracy of ± 0.01 m^2.
- *Volume of the inner vessel:* It is assumed an accuracy of ± 0.01 l or ± 0.00001 m^3.
- *Accuracy of Logger readings, operated between - 25 °C to + 50 °C, as given by the manufacturer:*
  - Maximum logger contribution to type T thermocouple errors (uncompensated): ± 0.9°C.
  - Voltage reading resolutions for single and differential measurements:

Table A1: Resolutions for single and differential measurements of the CR1000 Logger

Range	Scale	Resolution for Single Measurement	Resolution for Differential Measurement
1	± 2.5 mV	0.67 µV	0.33 µV
2	± 7.5 mV	2.0 µV	1.0 µV
3	± 25 mV	6.7 µV	3.33 µV
4	± 250 mV	66.7 µV	33.3 µV
5	± 2500 mV	667 µV	333 µV
6	± 5000 mV	1333 µV	667 µV

  - Voltage reading accuracies for single and differential measurements:

Table A2: Accuracies for single and differential measurements of the CR1000 Logger

Logger Temperature:	- 25 to + 50 °C
Scale Uncertainty	± 0.12 %
Long Term Stability	± 0.25 %
Differential Offset	± 0.02 %
Noise	0.34 µV RMS (negligible)

- *Calculation of RMS uncertainties:*

1. Temperature measurement uncertainty, $\sigma(T)$:

$$\sigma(T) = \sqrt{\sigma^2_{thermocouple}(T) + \sigma^2_{Logger}(T)} = \sqrt{0.5^2 + 0.9^2} = \pm\ 1.030\ ^\circ\text{C} \approx \pm 1\ ^\circ\text{C} \quad \text{(A1)}$$

2. Volume per aperture area measurement uncertainty, $\sigma(V_T/A_a)$:

$$\sigma(V_T / A_a) = \sqrt{\sigma^2(V_T) + \sigma^2(A_a)} = \sqrt{0.01^2 + 0.01^2} = \pm\ 0.014\,\text{lm}^{-2}$$

3. Irradiation measurement percent uncertainty, $\sigma_{\%}(Q_R)$:

The pyranometer has sensitivity of 17.29 $\mu V \cdot W^{-1} \cdot m^2$, so for intensities between 0 – 145 $W \cdot m^{-2}$ the logger range 1 is used, for intensities between 146 – 434 $W \cdot m^{-2}$ the logger range 2 is used, while for greater intensities the logger range 3 finally used. It is noted that the measurements for the radiation intensities have been made differentially. The total solar radiation intercepted by the aperture surface A_a (m^2) of the system during the time interval Δt_D (i.e. 43,200 s) from the startup time $t_{i,D}$ (~ 6:30 in the morning) till the end time $t_{f,D}$ (~ 18:30 in the afternoon, as solar noon occurs at about 12:30 pm), is given by the parameter Q_R (J), which is determined by the integration of the solar radiation intensity $G(t)$ over the time interval Δt_D:

$$Q_R = A_a \cdot \int_{t_{i,D}}^{t_{f,D}} G(t) \cdot dt \quad \text{(A2)}$$

So the RMS percentage uncertainty of Irradiation measurement can be expressed as:

$$\sigma_{\%}(Q_R) = \sqrt{\sigma^2_{\%\,\text{daily uncertainty}} + \left(\sigma_{\%\,\text{Logger Scale Uncertianty}} + \sigma_{\%\,\text{Logger Long Term}}\right)^2 + \sigma^2_{\%\,\text{apperture accuracy}}} \quad \text{(A3)}$$

Using the values (Table A2) of 0.12 % for Logger Scale Uncertainty, 0.25 % for Logger Long Term Stability and supposing pyranometer daily uncertainty $\sigma_{\%\,\text{daily uncertainty}} = \pm\ 5\%$, then for mean irradiation intensities *G*, $\sigma_{\%}(Q_R) = \pm\ 5.014$ % as calculated by (A3). As it is evident the Logger contribution to RMS error is negligible, which is dominated by the daily uncertainty of pyranometer error.

4. Pressure measurement percent uncertainty, $\sigma_{\%}(P)$:

The pressure transducer sensor PMP 4311 operates in the range between 0.2 to 4,500 Volts DC according to the relation $P = 2.325 \cdot V - 465$, where V (in mV) is the voltage output of the sensor with accuracy ± 1 %. The percent RMS uncertainty on P is then calculated as:

$$\sigma_{\%}(P) = \frac{\partial P}{\partial V} \cdot \sigma_{\%}(V) = 2.325 \cdot \sigma_{\%}(V) = \pm 2.325\ \% \tag{A4}$$

5. Calculation of percent uncertainty in useful energy $\sigma_{\%}(Q_{w,inner})$:

The useful energy output is calculated as $Q_{w,inner} = M_{w,inner} \cdot \overline{C}_{p,w} \cdot (T_{f,D} - T_{i,D})$, where:

$$M_{w,inner} = \rho \cdot V_{T,inner} \tag{A5}$$

$V_{T,inner}$	Volume of the inner vessel	m^3
ρ	Water density at temperature T	$kg \cdot m^{-3}$
$\overline{C}_{p,w}$	Mean (T_o, T_i) water specific heat capacity	$kJ \cdot kg^{-1} \cdot K^{-1}$
$T_{i,D}$, $T_{f,D}$	Initial and final water temperatures	K

The percent RMS uncertainty on $Q_{w,inner}$ is then calculated as:

$$\sigma_{\%}\left(Q_{w,inner}\right) = \sqrt{\sigma_{\%}^{2}\left(V_{T,inner}\right) + \sigma_{\%}^{2}(\rho) + \sigma_{\%}^{2}\left(\overline{c}_{p,w}\right) + \sigma_{\%}^{2}\left(T_{f,D} - T_{i,D}\right)} \tag{A6}$$

The density and the specific heat capacity of water are calculated, according to ISO-9459 and [25], with the relations:

$$\rho(\theta) = 1000,67 - 7,3845 \times 10^{-2}\theta - 3,547 \times 10^{-3}\theta^2 \ \ kg \cdot m^{-3}, \tag{A7}$$

$$\overline{c}_p(\theta_1, \theta_2) = 4,20028 - 5,048 \times 10^{-4}(\theta_1 + \theta_2) + 4,097 \times 10^{-6}\left[\left(\theta_1 + \theta_2\right)^2 - \theta_1\theta_2\right] \ kJ \cdot kg^{-1} \cdot K^{-1}, \tag{A8}$$

with θ, θ_1, θ_2, in °C. The percent uncertainty of ρ, $\overline{c}_{p,w}$ are expressed as:

$$\sigma_{\%}(\rho) = \frac{\partial \rho}{\partial \theta}\sigma_{\%}(\theta),\ \sigma_{\%}\left(\overline{c}_{p,w}\right) = \sqrt{\left(\frac{\partial \overline{c}_{p,w}}{\partial \theta_1}\sigma_{\%}(\theta_1)\right)^2 + \left(\frac{\partial \overline{c}_{p,w}}{\partial \theta_2}\sigma_{\%}(\theta_2)\right)^2} \tag{A9}$$

Where:

$$\frac{\partial \rho}{\partial \theta} = -7,3845\times10^{-2} - 7,094\times10^{-3}\theta \quad \text{(A10)}$$

$$\frac{\partial \overline{c}_{p,w}}{\partial \theta_1} = -5,048\times10^{-4} + 4,097\times10^{-6}\left(2\theta_1 + \theta_2\right) \quad \text{(A11)}$$

$$\frac{\partial \overline{c}_{p,w}}{\partial \theta_2} = -5,048\times10^{-4} + 4,097\times10^{-6}\left(2\theta_2 + \theta_1\right) \quad \text{(A12)}$$

So, calculating the percent uncertainty of ρ, $\overline{c}_{p,w}$, computing the uncertainties $\sigma_{\%}\left(T_{f,D}-T_{i,D}\right)$ from the relation (A1) and taking into account the $\sigma_{\%}\left(V_{T,inner}\right)$, the percent uncertainty $\sigma_{\%}\left(Q_{w,inner}\right)$ is extracted by the relation (A7). It is found that $\sigma_{\%}\left(Q_{w,inner}\right)$ uncertainty is dominated by $\sigma_{\%}\left(T_{f,D}-T_{i,D}\right)$ and $\sigma_{\%}\left(V_{T,inner}\right)$, while the contribution of all other sources of uncertainties can be considered negligible.

6. Calculation of percent uncertainty on system mean daily efficiency $\sigma_{\%}(\eta_D)$.

The system mean daily efficiency is calculated as $\eta_D = Q_{w,inner} / Q_R$. So a percent RMS uncertainty is expressed as:

$$\sigma_{\%}\left(\eta_D\right) = \sqrt{\sigma_{\%}^{2}\left(Q_{w,inner}\right) + \sigma_{\%}^{2}\left(Q_R\right)} \quad \text{(A13)}$$

The $Q_{w,inner}$ and Q_R percent uncertainties are calculated by the relations (A6) and (A3), respectively.

7. Calculation of percent uncertainty on system thermal losses $\sigma_{\%}$ (Us).

The system thermal losses coefficient is calculated as:

$$U_S = \left[\left(\rho\cdot\overline{C}_{p,w}\cdot V_{T,inner}\right)/\Delta t_N\right]\cdot\ln\left[\left(T_{i,N}-T_{a,N}\right)/\left(T_{f,N}-T_{a,N}\right)\right] \quad \text{(A14)}$$

The percent RMS uncertainty on U_S, taking also into consideration the all above, is then calculated as:

$$\sigma_{\%}\left(U_S\right) = \sqrt{\sigma_{\%}^{2}\left(V_{T,inner}\right) + \sigma_{\%}^{2}\left(\rho\right) + \sigma_{\%}^{2}\left(\overline{c}_{p,w}\right) + \sigma_{\%}^{2}\left(T_{i,N}-T_{a,N}\right) + \sigma_{\%}^{2}\left(T_{f,N}-T_{a,N}\right) + \sigma_{\%}^{2}\left(\Delta t_N\right)} \quad \text{(A15)}$$

For the extraction of the above uncertainty propagation analysis, the influence of uncertainty on coefficients in equations (A8) and (A9), uncertainty on Logger timing (sampling intervals) and inertia of sensors were considered negligible.

Highlights

- Heat diode mechanism in heating of an ICS solar water heater.
- Effect of the partial vacuum in the process of heating and retention of heat.
- Effective daily and night operation of the ICS system.
- Comparative experimental study between the ICS device and a FPTU.